Learning-Based Force Control of a Surgical Robot for Tool-Soft Tissue Interaction

Qinyuan Ren , *Senior Member, IEEE*, Wenxin Zhu, *Student Member, IEEE*,
Zhao Feng , and Wenyu Liang , *Member, IEEE*

Abstract—**Nowadays, robots are increasingly used in various surgery applications. Meanwhile, in many of these applications, the operation tools of surgical robots need to be in contact with human soft tissues. Furthermore, this tool-soft tissue interaction brings great challenges to robot control and system performance due to the nonlinearity, viscoelasticity, and uncertainties of the soft environment. To address these challenges and achieve the desired interaction behavior, a learning-based force controller for a surgical robot, which consists of a feedforward plus feedback controller, a radial basis function neural network-based controller, and an adaptive proportional–integral-type sliding mode control-based compensator, is presented in this letter. To display the stability of the proposed controller, the control system of the robot is analyzed through the Lyapunov method. Finally, several experiments are carried out in the robot prototype and the results illustrate that good tracking performance and guaranteed robustness can be obtained by the proposed controller.**

Index Terms—**Force control, robust/adaptive control, medical robots and systems.**

I. INTRODUCTION

IN MANY robotic surgery applications, such as nasal surgery [1], eye surgery [2], ear surgery [3], laparoscopic surgery [4], and minimally invasive surgery [5]–[7], where the operation tools (e.g., needles) need to be in contact with human soft tissues. To enhance the performance of the robotic systems during such tool-soft tissue interaction, recently, force control is widely adopted. For example, in [8], a force control approach was employed to assist the surgeon by applying precise contact force for the beating heart during the surgical operation. In [9], a hybrid motion/force control was designed for a continuum robot to regulate its contact force with the object surface. In [10], a 6-degree-of-fredom (6-DoF) robotic arm was used for automatic ultrasound scanning with force feedback. In [11], an adaptive control of the sclera force was utilized to achieve the safe robot-assisted retinal surgery. In [12], a fuzzy proportional–integral–derivative (PID) controller was proposed for a vascular interventional surgical robot. These notable examples have proved that force control can improve both the effectiveness and safety of the surgical procedure and possibly alleviates postoperative pain for the patients. Significantly, force control is crucial to the success of the surgical operation using surgical robots/devices, which can help the system to maintain stable contact with the soft tissue as well as to achieve a successful force feedback-based robotic surgery. But today, the use of force control for complex physiological motion remains a challenge due to the difficulty of accurately modelling the tool-soft tissue interaction.

From a perspective of cybernetics, modelling the tool-soft tissue interaction is critical to the force controller design. The commonly-used interaction models can be classified into two categories, namely finite element method-based (FEM-based) models and analytical models. Despite the accuracy of the former models, applying FEM-based models into real-time control is still under research. The analytical models can be regarded basis for the model-based controller design, but an accurate analytical model, describing the interaction of the tool-soft tissue, is very hard to be obtained because soft tissues are usually nonlinear, viscoelastic, and the tool operation circumstances are always unforeseen. Therefore, most of the current analytical models adopted for the force control of the surgical robots are greatly simplified and robust controllers are utilized in many studies to compensate the model uncertainties. In [13], the interaction between a hand-held surgical instrument and a living heart was simply described as a series of damping dashpots–springs, and a PI force controller was then employed to enhance the robustness of the control system. In [14], a force sensor-free force control based on position and a generalized Kelvin–Voigt contact model was proposed for tendon-driven ablation catheters. In [15] and [16], Dominici *et al.* introduced a linear predictive force control approach to compensate heart physiological motion. In [17], Zarrouk *et al.* proposed a model reference adaptive controller to adapt to the changing operation circumstance.

To address the issues on tool-soft tissue interaction during the robotic surgery, this letter presents a novel learning-based force control approach for a compact size surgical robot. In this robotic system, a linear ultrasonic motor (USM), which is a piezoelectric actuator, is adopted to drive a slim surgical tool with high precision motion. Thus, this system can be applied to many minimally invasive surgeries, such as automatic injection and implant insertion [18], where the tool-soft tissue interaction is involved. This interaction, in our study, is firstly described by a rough analytical model, namely Hunt–Crossley (HC) nonlinear model,

Fig. 1.   USM-driven device for robotic surgery.

Fig. 2.   System model that integrates the nonlinear model of the interaction with the model of the robotic system.

and then refined by a leaning mechanism through a radial basis function neural network (RBFNN). Moreover, to compensate the residual error of the proposed RBFNN-based controller and further improve the system robustness, an adaptive compensator based on a PI-type sliding mode controller (SMC) is employed. It is worth noting that the proposed RBFNN is designed to deal with most of the nonlinearites of the robot system and the SMC mainly plays the role as a compensator. Then, the required control effort of the SMC-based compensator can be less when it is used with the RBFNN. Hence, the chattering effect in the SMC because of the use of sign function, can be reduced in this system due to adopting the RBFNN. Furthermore, owing to the universal function approximation ability and online learning mechanism of the proposed controller, the robot control system can obtain good force tracking performance and robustness while the surgical tool is interacting with soft tissues.

The main contributions of this letter are listed as follows: (i) The HC nonlinear model is considered and integrated with the model of a USM-driven surgical robot and thus a complete model, consisting of the tool-soft tissue interaction and the robotic motion system, is built. It offers a new model for interaction analysis and control design. (ii) Based on the system model, a learning-based force control approach is analytically deduced and constructed to deal with the system nonlinearities, where a RBFNN-based controller and an adaptive PI-type SMC are employed. (iii) The effectiveness and performance of the proposed method are tested via experiments with a practical surgical robot, where the robotic system is applied to the contact force tracking on the soft membrane that is with similar properties to human tissue (e.g., tympanic membrane).

The rest of the paper is organized as follows. The system description and modelling are presented and discussed in Section II. Section III details the design of the learning-based force controller. Then, the validness of the proposed controller is proved through several experiments and the results are provided in Section IV. Finally, Section V gives a conclusion.

II. SYSTEM DESCRIPTION AND MODELLING

A USM-driven device developed for robotic surgery is shown in Fig. 1. It consists of a linear USM (with minimum incremental displacement of $0.3~\mu$m) for generating precise motions, a small size force sensor for measuring the interaction force between
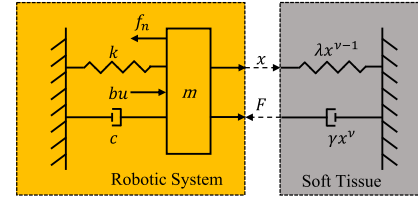
the robotic system/tool and environment, and a retraction mechanism for moving the surgical tool (e.g., needle) in or out from the hollow holder. Significantly, a linear encoder is embedded in the USM to measure the USM's motion. This robotic system is mainly designed for surgical operation and micromanipulation with precise motions such as automatic injection and implant insertion [18].

In general, the USM-driven robotic system can be represented as a combination of a second-order linear system and nonlinearities (including hysteresis and friction) [19]. The model of this robotic system is described by

$$m\ddot{x} + c\dot{x} + kx + f_n = bu - F, \qquad (1)$$

where k, b, m are the stiffness coefficients, damping parameters and the effective mass, respectively. x is the position of the tool, $\dot{x}$ is the velocity, and $\ddot{x}$ is the acceleration. Moreover, u denotes the control input signal to the USM through an electromechanical ratio b of the system. f_n represents the nonlinearities which is related to x and $\dot{x}$, and it can be further rewritten as $f_n(x, \dot{x})$ which is bounded (i.e., $|f_n(x, \dot{x})| \leq \Theta_f$ with $\Theta_f > 0$). Lastly, F is the interaction force between the robotic system/tool and environment which can be obtained from the mounted force sensor. It also assumes that F is bounded (i.e., $|F| \leq \Theta_F$ with $\Theta_F > 0$).

The main contacting environment for this robotic system is the soft tissue and which is a type of soft environment. To describe such dynamics between the system and the soft environment which are generally nonlinear and viscoelastic, many linear compliant contact models, such as Maxwell model, Kelvin–Voigt model, Kelvin–Boltzmann model have been developed and used [3], [20], [21]. However, the experimental results reported in [22], [23] show that soft materials such as human tissue/organ can be more accurately modelled by the HC nonlinear model. Here, the HC nonlinear model is used to describe the interaction between the robotic system and the soft tissue. Fig. 2 illustrates the contact model while the USM-driven robotic system is in contact with the environment. When $x \geq 0$, the HC contact model can be represented by

$$F = \lambda x^\nu + \gamma x^\nu \dot{x}, \qquad (2)$$

where λ, γ and ν are model parameters, and $\lambda x^{\nu-1}$ and γx^ν are the position-dependent stiffness and damping, respectively.

From (2), we can have the time derivative of F,

$$\dot{F} = \nu\lambda x^{\nu-1}\dot{x} + \nu\gamma x^{\nu-1}\dot{x}^2 + \gamma x^\nu \ddot{x}. \qquad (3)$$

Then, the acceleration $\ddot{x}$ can be estimated from the contact model by the following equation,

$$\ddot{x} = \gamma^{-1}x^{-\nu}(\dot{F} - \nu\lambda x^{\nu-1}\dot{x}) - \nu x^{-1}\dot{x}^2. \qquad (4)$$

As can be seen, $\ddot{x}$ can be represented by a nonlinear model related to x, $\dot{x}$, and $\dot{F}$, which is

$$\ddot{x} = g(x, \dot{x}, \dot{F}). \tag{5}$$

Substitute (5) into (1) and let $g_n(x, \dot{x}, \dot{F}) = mg(x, \dot{x}, \dot{F})$, we have

$$g_n(x, \dot{x}, \dot{F}) + c\dot{x} + kx + f_n(x, \dot{x}) = bu - F. \tag{6}$$

Denote the linear part of this system as a function of x and $\dot{x}$, i.e., $h(x, (\dot{x})) \triangleq c\dot{x} + kx$. Thus, the model (6) becomes

$$g_n(x, \dot{x}, \dot{F}) + h(x, \dot{x}) + f_n(x, \dot{x}) = bu - F. \tag{7}$$

Significantly, the model parameters c and k are also unknown.

In this letter, the objective is to develop a precise force tracking controller for the USM-driven robotic system when it is in contact with the soft tissue (e.g., soft thin membrane).

III. CONTACT FORCE CONTROLLER DESIGN

Based on the model (7), a perfect control law u^* shown in (8) is designed such that the contact force F can track the desired force reference F_d.

$$u^* = b^{-1}\Bigg[g_n(x, \dot{x}, \dot{F}) + h(x, \dot{x}) + f_n(x, \dot{x})$$
$$+ F_d + \mu e_F + \alpha \dot{e}_F + \beta \int e_F d\tau\Bigg], \tag{8}$$

where $e_F = F_d - F$ is the force tracking error, β is the controller parameter to be designed.

Property 1: The force tracking error e_F of the robotic system converges to zero as time goes to infinity if the perfect control law (8) is applied and the controller parameter β is designed properly such that $s^2 + k_\mu s + k_\beta$ is Hurwitz stable, where $k_\mu = (1 + \mu)/\alpha$ and $k_\beta = \beta/\alpha$.

Proof of Property 1: Substitute (8) into (7), we have

$$0 = F_d - F + \mu e_F + \alpha \dot{e}_F + \beta \int e_F d\tau. \tag{9}$$

Then, it yields

$$\dot{e}_F + \frac{1 + \mu}{\alpha} e_F + \frac{\beta}{\alpha} \int e_F d\tau = 0. \tag{10}$$

Since $s^2 + k_\mu s + k_\beta$ is designed to be Hurwitz stable, thus

$$\lim_{t \to \infty} e_F(t) = 0. \tag{11}$$

This implies that e_f converges to 0 as time goes to infinity. ∎

As can be seen in (8), the perfect control law can be divided into two parts, namely, $u^* = u_n^* + u_F^*$ with

$$u_n^* = b^{-1}[g_n(x, \dot{x}, \dot{F}) + h(x, \dot{x}) + f_n(x, \dot{x})], \tag{12}$$

$$u_F^* = b^{-1}\Bigg[F_d + \mu e_F + \alpha \dot{e}_F + \beta \int e_F d\tau\Bigg], \tag{13}$$

where u_n^* is highly related to the system nonlinearities and the unknown but bounded model uncertainties, and u_F^* can be considered as a feedforward plus feedback force controller.

From (13), it can be found that u_F^* is easy to achieve as F_d is known and $e_F = F_d - F$ can be obtained from the force sensor. On the other hand, u_n^* is difficult to obtain due to the
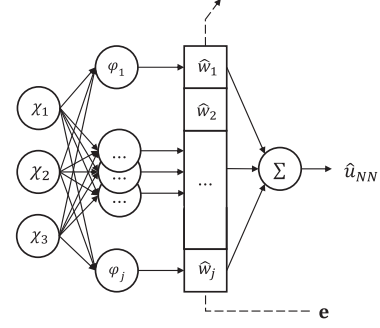
Fig. 3. RBFNN with an input layer, a hidden layer, and an output layer.

nonlinearities and uncertainties. Therefore, we aim to design a controller that is able to approximate this part of the perfect controller u_n^* as shown in (12).

A. Radial Basis Function Neural Network-Based Controller

From (12), u_n^* is actually a nonlinear controller that relates to the system outputs x, $\dot{x}$, and $\dot{F}$. In this case, an RBFNN is a good solution to approximate such a nonlinear function.

Fig. 3 illustrates the RBFNN adopted in this letter, and the RBFNN consists of an input layer, a hidden layer, and an output layer. The input layer receives the input vector. The hidden layer comprises a set of radial basis functions (RBFs), whose inputs are the linear combinations of the weight vector and the input vector. The output layer outputs the linear combination of the RBFs. The RBFNN can be expressed as

$$u_{NN} = \mathbf{w}^T \boldsymbol{\varphi}(\boldsymbol{\chi}) \tag{14}$$

with

$$\mathbf{w} = \begin{bmatrix} w_0 & w_1 & \cdots & w_j \end{bmatrix}^T, \tag{15}$$

$$\boldsymbol{\varphi}(\boldsymbol{\chi}) = \begin{bmatrix} \varphi_0 & \varphi_1(\boldsymbol{\chi}) & \varphi_2(\boldsymbol{\chi}) & \cdots & \varphi_j(\boldsymbol{\chi}) \end{bmatrix}^T, \tag{16}$$

where $\varphi_0 = 1$, $\boldsymbol{\chi}$ is the input vector, $\mathbf{w}$ is the vector of the neural network weights with the first element as ideal threshold and $\boldsymbol{\varphi}(\boldsymbol{\chi})$ is the activation function containing the RBF.

Each RBF describes the distance between a given input vector and a predefined center vector. The following RBF is used in this letter,

$$\varphi_i = \exp\left(-\frac{||\boldsymbol{\chi} - \boldsymbol{\mu}_i||^2}{\sigma_i^2}\right), \tag{17}$$

where σ_i is a coefficient, $\boldsymbol{\mu}_i$ is the center for the i-th neuron.

All the parameters of the RBFNN will be tuned, so we can have the estimated network as shown below:

$$\hat{u}_{NN} = \hat{\mathbf{w}}^T \boldsymbol{\varphi}(\boldsymbol{\chi}), \tag{18}$$

where $\hat{\mathbf{w}}^T$ is the estimated weight vector.

Assume that an optimal weight vector $\bar{\mathbf{w}}^T$ exists for the RBFNN and the error between the optimal weight vector and the estimated weight vector is defined as $\tilde{\mathbf{w}}^T = \bar{\mathbf{w}}^T - \hat{\mathbf{w}}^T$, then we have

$$\hat{u}_{NN} = (\bar{\mathbf{w}}^T - \tilde{\mathbf{w}}^T)\boldsymbol{\varphi}(\boldsymbol{\chi}). \tag{19}$$

Combine (13) and (19) to form the controller, we have

$$\bar{u} = u_F + \hat{u}_{NN} = u_F^* + \hat{\mathbf{w}}^T \boldsymbol{\varphi}(\boldsymbol{\chi}), \tag{20}$$

where $u_F = u_F^*$.

Feed (13) and (20) into (7) as the control input, we have

$$\dot{e}_F = -k_\mu e_F - k_\beta \int e_F d\tau - \frac{b}{\alpha} \hat{\mathbf{w}}^T \boldsymbol{\varphi}(\boldsymbol{\chi})$$

$$+ \frac{b}{\alpha}[g_n(x, \dot{x}, \dot{F}) + h(x, \dot{x}) + f_n(x, \dot{x})]$$

$$= -k_\mu e_F - k_\beta \int e_F d\tau + \frac{b}{\alpha}(u_n^* - \hat{u}_{NN}), \qquad (21)$$

and which can be further rewritten as

$$\dot{e}_F = -k_\mu e_F - k_\beta \int e_F d\tau + \frac{b}{\alpha}[u_n^* - (\bar{\mathbf{w}}^T - \tilde{\mathbf{w}}^T)\boldsymbol{\varphi}(\boldsymbol{\chi})]$$

$$= -k_\mu e_F - k_\beta \int e_F d\tau + b_\alpha[\delta_u + \tilde{\mathbf{w}}^T \boldsymbol{\varphi}(\boldsymbol{\chi})], \qquad (22)$$

where $\delta_u = u_n^* - \bar{\mathbf{w}}^T \boldsymbol{\varphi}(\boldsymbol{\chi})$ is the difference between the perfect controller and the optimal RBFNN controller, which is bounded (i.e., $|\delta_u| \le \Delta_u$), and $b_\alpha = b/\alpha$.

Define $\epsilon = \delta_u + \tilde{\mathbf{w}}^T \boldsymbol{\varphi}(\boldsymbol{\chi})$, (22) is then represented by the following state-space model:

$$\dot{\mathbf{e}} = A\mathbf{e} + \mathbf{B}\epsilon,$$

with $\quad A = \begin{bmatrix} -k_\mu & -k_\beta \\ 1 & 0 \end{bmatrix}, \quad \mathbf{B} = \begin{bmatrix} b_\alpha & 0 \end{bmatrix}^T, \qquad (23)$

where $\mathbf{e} = \begin{bmatrix} e_F & \int e_F d\tau \end{bmatrix}^T$. It is worth mentioning that ϵ is the residual error exists in the control system (23).

Meanwhile, an online tuning approach inspired from [24] and [25] is implemented to estimate the weights, and the learning law for the RBFNN is designed as follows:

$$\dot{\hat{\mathbf{w}}} = \kappa \mathbf{e}^T P \mathbf{B} \boldsymbol{\varphi}, \qquad (24)$$

where $\kappa > 0$ denotes the learning rate, P is the solution of $A^T P + PA = -Q$ with $Q > 0$, and $\boldsymbol{\varphi} = \boldsymbol{\varphi}(\boldsymbol{\chi})$.

B. Sliding Mode Control-Based Compensator

To compensate the residual error of the RBFNN-based controller and the remaining nonlinearities, a compensator based on the sliding mode technique is employed. The control law of the SMC is shown below.

$$u_s = \hat{\varrho}\,\text{sign}(\mathbf{e}^T P \mathbf{B}), \qquad (25)$$

where $\hat{\varrho}$ is the compensator gain to be designed, and $\text{sign}(\cdot)$ denotes the sign function. Remarkably, the PI-type sliding surface is employed in (25). The integral term introduced in the sliding mode control can offer the advantages of faster transient response with little steady-state error [26].

C. Overall Controller

Hence, by adding the SMC (25) into the controller (20), we have the overall controller as shown below.

$$u = u_F + \hat{\mathbf{w}}^T \boldsymbol{\varphi}(\boldsymbol{\chi}) + \hat{\varrho}\,\text{sign}(\mathbf{e}^T P \mathbf{B}). \qquad (26)$$

Furthermore, consider the overall controller u as an input to the system, (23) becomes

$$\dot{\mathbf{e}} = A\mathbf{e} + \mathbf{B}(\epsilon - u_s). \qquad (27)$$

Theorem 1: The stability of the control system is guaranteed and the force error converges to zero under the overall controller (26) with the learning law (24) and the sliding mode control-based compensator gain $\hat{\varrho}$ is designed properly such that it fulfills one of the following two conditions:

i) $\hat{\varrho}$ is a designed positive constant with $\hat{\varrho} \ge \Delta_u$; or

$$ii) \qquad \dot{\hat{\varrho}} = \text{Proj}(\hat{\varrho}, \rho|\mathbf{e}^T P \mathbf{B}|) \qquad (28)$$

where $\text{Proj}(\cdot)$ is a projection operator as given below:

$$\text{Proj}(\hat{\varrho}, \phi) = \begin{cases} \phi, & \text{if } l(\hat{\varrho}) \le 0 \\ \phi, & \text{if } l(\hat{\varrho}) > 0 \text{ and } \bar{l}(\hat{\varrho})\phi \le 0 \\ \left[I - \frac{l(\hat{\varrho})\bar{l}(\hat{\varrho})l(\hat{\varrho})^T}{||\bar{l}(\hat{\varrho})||^2} \right]\phi, & \text{otherwise} \end{cases}, \qquad (29)$$

with $\phi = \rho|\mathbf{e}^T P \mathbf{B}|$, $l(\hat{\varrho}) = \frac{\hat{\varrho}^T \hat{\varrho} - \Theta_\varrho^2}{v^2 + 2v\Theta_\varrho}$, $\bar{l}(\hat{\varrho}) = \frac{\partial l(\hat{\varrho})}{\partial \hat{\varrho}}$, where Θ_ϱ is the maximum value of $|\hat{\varrho}|$ (i.e., $|\hat{\varrho}| \le \Theta_\varrho$) and v is an arbitrary positive constant.

Proof of Theorem 1: Define a Lyapunov function as follows,

$$V = \frac{1}{2}\mathbf{e}^T P \mathbf{e} + \frac{1}{2\kappa}\tilde{\mathbf{w}}^T \tilde{\mathbf{w}} + \frac{1}{2\rho}\tilde{\varrho}^2, \qquad (30)$$

where $\tilde{\varrho} = \varrho^* - \hat{\varrho}$ is the error between the ideal compensator gain $\varrho^* = \Delta_u$ and the estimated gain $\hat{\varrho}$.

Following that, derivate of V with respect to time is obtained as

$$\dot{V} = \frac{1}{2}\dot{\mathbf{e}}^T P \mathbf{e} + \frac{1}{2}\mathbf{e}^T P \dot{\mathbf{e}} + \kappa^{-1}\tilde{\mathbf{w}}^T \dot{\tilde{\mathbf{w}}} + \rho^{-1}\tilde{\varrho}\dot{\tilde{\varrho}}$$

$$= \frac{1}{2}\dot{\mathbf{e}}^T P \mathbf{e} + \frac{1}{2}\mathbf{e}^T P \dot{\mathbf{e}} - \kappa^{-1}\tilde{\mathbf{w}}^T \dot{\hat{\mathbf{w}}} - \rho^{-1}\tilde{\varrho}\dot{\hat{\varrho}}. \qquad (31)$$

Substitute the error model (27) into (31), we have

$$\dot{V} = \frac{1}{2}(\mathbf{e}^T A^T P \mathbf{e} + \mathbf{e}^T P A \mathbf{e}) + \mathbf{e}^T P \mathbf{B}(\epsilon - u_s)$$

$$- \kappa^{-1}\tilde{\mathbf{w}}^T \dot{\hat{\mathbf{w}}} - \rho^{-1}\tilde{\varrho}\dot{\hat{\varrho}}$$

$$\le -\frac{1}{2}\mathbf{e}^T Q \mathbf{e} + \mathbf{e}^T P \mathbf{B}(\epsilon - u_s)$$

$$- \kappa^{-1}\tilde{\mathbf{w}}^T \dot{\hat{\mathbf{w}}} - \rho^{-1}\tilde{\varrho}\dot{\hat{\varrho}}. \qquad (32)$$

Substitute the learning law (24) into (32), (32) becomes

$$\dot{V} \le -\frac{1}{2}\mathbf{e}^T Q \mathbf{e} + \mathbf{e}^T P \mathbf{B}(\epsilon - u_s) - \mathbf{e}^T P \mathbf{B}\tilde{\mathbf{w}}^T \boldsymbol{\varphi} - \rho^{-1}\tilde{\varrho}\dot{\hat{\varrho}}. \qquad (33)$$

For condition (i), we have $\dot{\hat{\varrho}} = 0$ as $\hat{\varrho}$ is a constant, and thus (33) becomes

$$\dot{V} \le -\frac{1}{2}\mathbf{e}^T Q \mathbf{e} + \mathbf{e}^T P \mathbf{B}(\epsilon - u_s) - \mathbf{e}^T P \mathbf{B}\tilde{\mathbf{w}}^T \boldsymbol{\varphi}$$

$$= -\frac{1}{2}\mathbf{e}^T Q \mathbf{e} + \mathbf{e}^T P \mathbf{B}(\epsilon - \tilde{\mathbf{w}}^T \boldsymbol{\varphi}) - \hat{\varrho}|\mathbf{e}^T P \mathbf{B}|$$

$$\le -\frac{1}{2}\mathbf{e}^T Q \mathbf{e} + |\mathbf{e}^T P \mathbf{B}||\delta_u| - \hat{\varrho}|\mathbf{e}^T P \mathbf{B}|. \qquad (34)$$

As $\hat{\varrho}$ is designed to be large enough that $\hat{\varrho} \ge \Delta_u$ and $\Delta_u \ge |\delta_u|$, then we have $|\delta_u| - \hat{\varrho} \le 0$, and

$$\dot{V} \le -\frac{1}{2}\mathbf{e}^T Q \mathbf{e} \le -\frac{1}{2}\lambda_{\min}\mathbf{e}^T \mathbf{e} = -\frac{1}{2}\lambda_{min}||\mathbf{e}||^2. \qquad (35)$$

For condition (ii), it should be noted that the projection operator holds the following property.

$$\text{Proj}(\hat{\varrho}, \rho|\mathbf{e}^T P \mathbf{B}|) \geq \rho|\mathbf{e}^T P \mathbf{B}|. \qquad (36)$$

Then, substitute the SMC adaptive law (28) and use the property of the projection operator (36) into (33), we have

$$\dot{V} \leq -\frac{1}{2}\mathbf{e}^T Q \mathbf{e} + \mathbf{e}^T P \mathbf{B}(\epsilon - u_s) - \mathbf{e}^T P \mathbf{B}\tilde{\mathbf{w}}^T \boldsymbol{\varphi} - \hat{\varrho}|\mathbf{e}^T P \mathbf{B}|$$

$$= -\frac{1}{2}\mathbf{e}^T Q \mathbf{e} + \mathbf{e}^T P \mathbf{B}(\epsilon - \tilde{\mathbf{w}}^T \boldsymbol{\varphi}) - (\hat{\varrho} + \tilde{\varrho})|\mathbf{e}^T P \mathbf{B}|$$

$$= -\frac{1}{2}\mathbf{e}^T Q \mathbf{e} + \mathbf{e}^T P \mathbf{B}\delta_u - \varrho^*|\mathbf{e}^T P \mathbf{B}|. \qquad (37)$$

Therefore, $\dot{V}$ can be further obtained as follows,

$$\dot{V} \leq -\frac{1}{2}\lambda_{min}\mathbf{e}^T \mathbf{e} + |\delta_u \mathbf{e}^T P \mathbf{B}| - \varrho^*|\mathbf{e}^T P \mathbf{B}|$$

$$= -\frac{1}{2}\lambda_{min}\mathbf{e}^T \mathbf{e} + (|\delta_u| - \Delta_u)|\mathbf{e}^T P \mathbf{B}| \qquad (38)$$

where λ_{min} is the minimum eigenvalue of Q.

Since it holds $|\delta_u| \leq \Delta_u$, we have the following inequality,

$$\dot{V} \leq -\frac{1}{2}\lambda_{min}||\mathbf{e}||^2. \qquad (39)$$

Because either condition can yield $\dot{V} \leq -\frac{1}{2}\lambda_{min}||\mathbf{e}||^2 \leq 0$ (i.e., the sign of $\dot{V}$ is not positive), it can be concluded that $\mathbf{e}$, $\tilde{\mathbf{w}}$, $\tilde{\varrho}$ are bounded and hence the control system is stable.

Furthermore, it can also be found that $\dot{\mathbf{e}}$ is bounded because $\mathbf{e}$, $\hat{\mathbf{w}}$, and u_s are bounded. Then, the following inequality can be obtained from (39),

$$\lim_{t \to \infty} \int_0^t \frac{1}{2}\lambda_{min}||\mathbf{e}||^2 d\tau \leq V(0) - V(\infty) \leq V(0), \qquad (40)$$

where the positive definiteness of V has been used.

According to the Barbalat's lemma, we have

$$\lim_{t \to \infty} ||\mathbf{e}|| = 0. \qquad (41)$$

As a result, the stability of the control system can be guaranteed and the force error $\mathbf{e}$ can converge to zero. ∎

Finally, the block diagram of the overall controller can be illustrated in Fig. 4.

IV. EXPERIMENTS AND RESULTS

Several experiments are carried out to verify the validness and performance of the proposed force controller. Fig. 5 illustrates the experimental setup.

The setup consists of the USM-driven device, a fixture holding a soft membrane that is made of Polyethylene (PE), an amplifier for the force sensor, a motor drive for the USM, a computer, a dSPACE DS1104 control card (put the control card into the computer and not shown in Fig. 5) and power supplies. In this setup, the PE soft membrane is used to simulate the soft tissue to be in contact with. The outputs of the embedded linear encoder in the USM and the mounted force sensor are acquired by the control card. Then, the control card implements the overall contact force controller with the sampling time of 1 ms, and the motor control signal calculated from the controller is outputted from the digital-to-analog converter (DAC) of the control card to the motor drive.
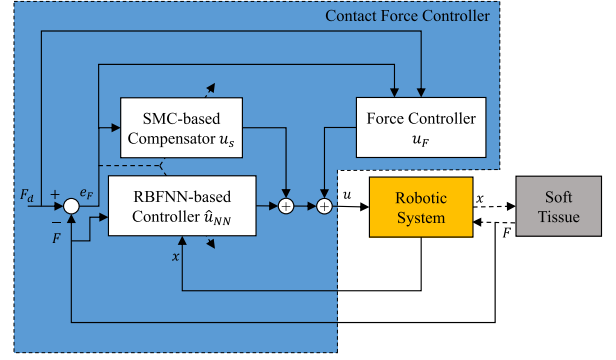
Fig. 4. Overall controller that consists of a force controller using feedforward plus feedback, a RBFNN-based controller, and an SMC-based compensator.
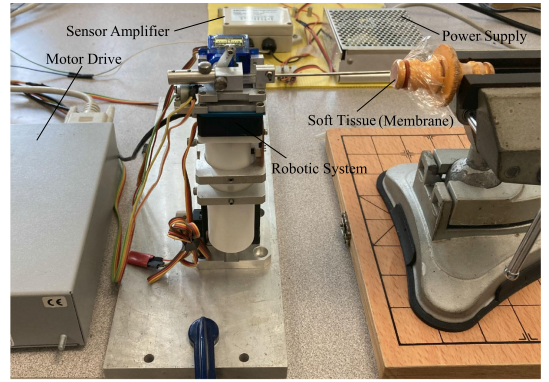
(a)
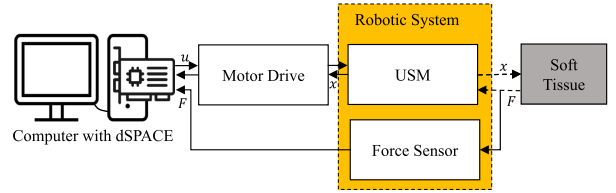
(b)

Fig. 5. Experimental system setup: (a) setup; (b) system block diagram.

A. Tracking Performance

Firstly, a periodic sinusoidal wave with the frequency of 0.2 Hz and the amplitude from 0 to 0.2 N are set as the force tracking reference in the experiment conducted on the experimental system setup. The tracking performance and the tracking error at 0.2 Hz sinusoidal wave are shown in Fig. 6.

According to the result, we can find out that the desired force trajectory can be tracked correctly using the proposed control system, where the root-mean-square error (RMSE) is 0.0032 N, the mean absolute error (MAE) is 0.0024 N, and the maximum absolute error (MaxAE) is 0.0112 N, respectively. Significantly, the MaxAE is 5.60% (less than 10%) of the reference's maximum value (0.2 N), which is very important to a surgical robot. This is because the MaxAE can result from the overshoot or undershoot which may cause discomfort or an injury on the patient when the overshoot is too large or lead to an unsuccessful operation.
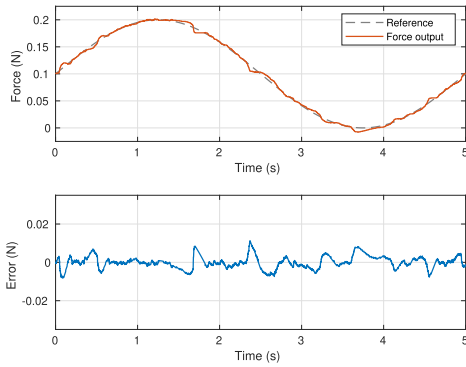
Fig. 6.   The proposed controller tracking performance at 0.2 Hz.
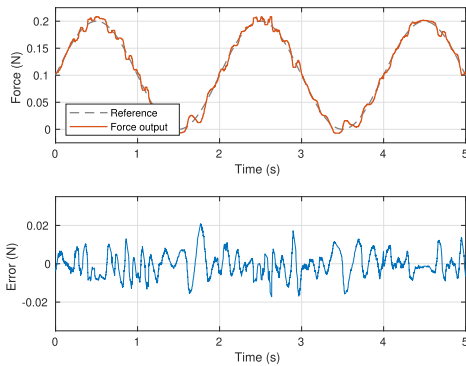
Fig. 7.   The proposed controller tracking performance at 0.5 Hz.
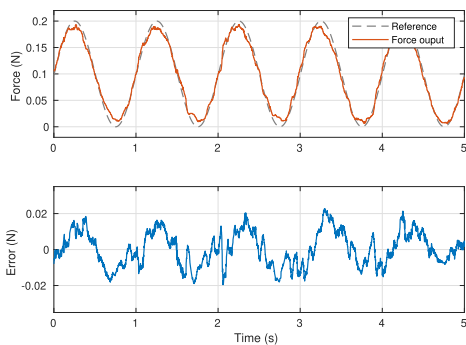
Fig. 8.   The proposed controller tracking performance at 1 Hz.

Next, another two experiments are conducted while another two different periodic sinusoidal waves with higher frequencies are set as the force tracking references and applied to the experimental system setup. These two periodic sinusoidal waves are with different frequencies of 0.5 Hz and 1 Hz, but the same amplitude of 0.2 N. Figs. 7 and 8 show the contact force control performance of the proposed controller.

According to the experimental results shown in the figures, the proposed control system is able to follow all the tracking references at different frequencies correctly. The RMSE, MAE, and MaxAE are 0.0065 N, 0.0051 N, and 0.0208 N at 0.5 Hz, respectively, while they are 0.0095 N, 0.0080 N, and 0.0228 N at 1 Hz, respectively. Significantly, the MaxAE can be maintained at around 10% of 0.2 N. Furthermore, the RMSEs and MAEs at
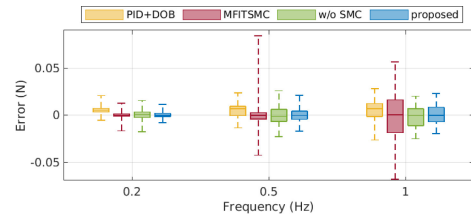
Fig. 9.   Force error boxplot of different controllers at different frequencies.

(a)

(b)

(c)
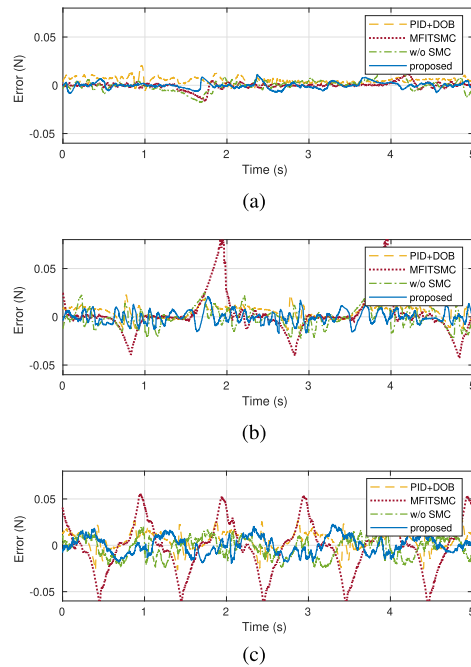
Fig. 10.   Force errors using different controllers at different frequencies: (a) 0.2 Hz; (b) 0.5 Hz; (c) 1 Hz.

all frequencies less than 0.01 N shows that the proposed force controller is able to obtain good force tracking performance, no matter the speed of the desired force trajectory is slow or fast.

B. Comparison Results

For comparison purposes, the following three force controllers: (i) PID controller plus disturbance observer (DOB) with a DOB bandwidth of 150 Hz [3], (ii) model-free integral terminal sliding mode control (MFITSMC), where fast finite-time integral terminal sliding mode technique and time-delayed estimation method are employed [27], and (iii) the proposed controller without SMC (w/o SMC) are applied to the USM-driven robotic system. Here, the parameters are determined first by the simulation results and then are tuned elaborately on the practical experimental setup with the trail and error method so that the anticipated performance can be obtained and the comparisons are suitably fair.

Fig. 9, Fig. 10, and Table I show the comparison results among those two force controllers and the proposed controller on different tracking references.

The experimental results listed in the table also illustrate clearly that the proposed controller is able to obtain the best

TABLE I
COMPARISON RESULTS OF SINGLE-LAYER MEMBRANE

	Error (N)	PID+DOB	MFITSMC	w/o SMC	proposed
0.2 Hz	RMSE	0.0061	0.0034	0.0059	0.0032
	MAE	0.0054	0.0022	0.0043	0.0024
	MaxAE	0.0206	0.0168	0.0179	0.0112
0.5 Hz	RMSE	0.0080	0.0233	0.0100	0.0065
	MAE	0.0067	0.0120	0.0079	0.0051
	MaxAE	0.0233	0.0874	0.0257	0.0208
1 Hz	RMSE	0.0113	0.0278	0.0110	0.0095
	MAE	0.0093	0.0213	0.0093	0.0080
	MaxAE	0.0278	0.0682	0.0252	0.0228

force tracking performance in terms of both RMSE and MaxAE at all frequencies.

At the lowest frequency (i.e., 0.2 Hz), all the three controllers can track the desired force trajectory well, but both MFITSMC and the proposed controller perform better force tracking performance than PID+DOB. Furthermore, the proposed controller can perform slightly smaller RMSE but over 33% improvement on MaxAE than MFITSMC.

However, as the frequency of the tracking references increases (i.e., frequency ≥ 0.5 Hz), the force tracking the performance of MFITSMC decreases significantly which MaxAEs are about three to four times than the proposed controller, although its median force error is still close to zero, while both PID+DOB and the proposed controller can still function well with smaller RMSEs and MaxAEs. This is because the time-delayed estimation used in MFITSMC is not able to compensate the sudden change of friction, where the friction is evident for this USM-driven robotic system. It also implies that the RBFNN-based controller can compensate the system nonlinearities well so that the proposed control system performance is not much affected by the sudden change of friction.

At the higher frequencies (i.e., 0.5 Hz, and 1 Hz), the MaxAEs while the proposed controller is applied are about 11% to 18% smaller than those while PID+DOB is applied. These improvements are mainly due to the good capability of nonlinear compensation by the designed RBFNN-based controller. Also, the smaller MaxAE can be beneficial to the surgical operations as smaller MaxAE can reduce the discomfort and the risk of injury to the patient.

Additionally, the results while using the proposed controller without SMC show that it can also track the desired force trajectories well which tracking performance is similar (at 0.5 Hz) or slightly better (at 0.2 and 1 Hz) to the PID+DOB. By comparing these results with the results while using the proposed controller (with SMC), it can be found that the performance is definitely improved which implies that the integration of SMC can further improve the tracking performance.

C. robustness

Lastly, to evaluate the robustness of the proposed controller, experiments are conducted on the same experimental system setup but with a thicker/stronger soft membrane, the two-layer soft membrane. It should be noted that the two-layer soft membrane's thickness is two times the thickness of the membranes used in the previous experiments.

Fig. 11 to Fig. 13 and Table II show the experimental results of the force tracking control using the proposed controller on the two-layer membrane while different sinusoidal waves are
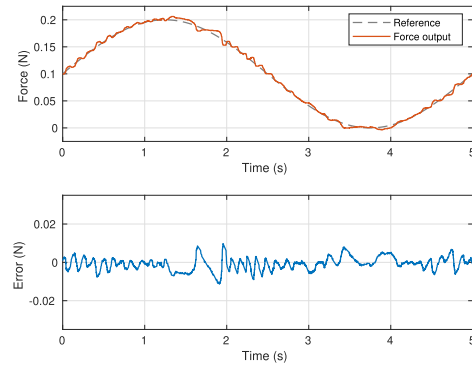
Fig. 11. The proposed controller tracking performance on two-layer soft membrane at 0.2 Hz.
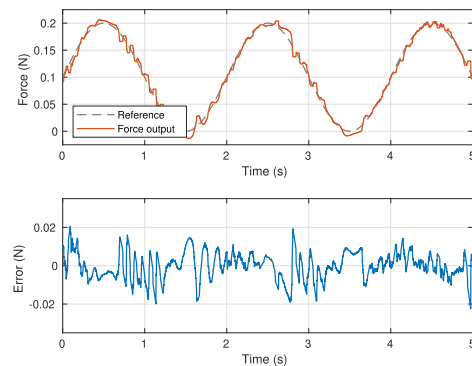
Fig. 12. The proposed controller tracking performance on two-layer soft membrane at 0.5 Hz.
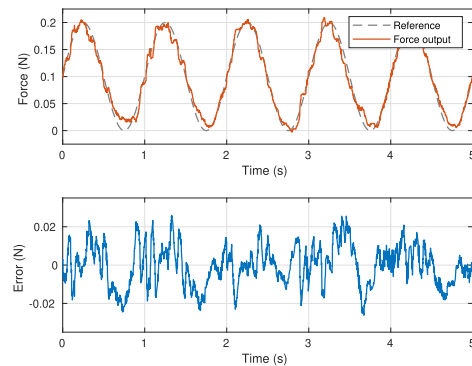
Fig. 13. The proposed controller tracking performance on two-layer soft membrane at 1 Hz.

TABLE II
COMPARISON RESULTS OF SINGLE-LAYER VS TWO-LAYER MEMBRANE

	Error (N)	single-layer	two-layer	changes vs single-layer
0.2 Hz	RMSE	0.0032	0.0035	9.38%
	MAE	0.0024	0.0027	12.50%
	MaxAE	0.0112	0.0113	0.89%
0.5 Hz	RMSE	0.0065	0.0071	9.23%
	MAE	0.0051	0.0055	7.84%
	MaxAE	0.0208	0.0225	8.17%
1 Hz	RMSE	0.0095	0.0106	11.58%
	MAE	0.0080	0.0086	7.50%
	MaxAE	0.0228	0.0261	14.47%

set as the tracking references. As can be seen from the figures, the system can still track the desired force trajectories well. By comparing the results on two-layer membrane to the results on single-layer membrane, the error increments are all within 15% where the RMSE's increments are even less than 10% at 0.2 Hz and 0.5 Hz, although the soft environment is two times in thickness.

Besides that, for the control efforts, the sum of the absolute values (in 5 s) of the RBFNN-based controller outputs (i.e., $\hat{u}_{NN}$) are 15.54, 38.13, and 67.63 at 0.2 Hz, 0.5 Hz, and 1 Hz, respectively, which are 21.35%, 84.59%, and 95.33% of the total nonlinear controller outputs $u_n = u_s + \hat{u}_{NN}$ in terms of their sum of the absolute values at different frequencies. At the higher frequencies (i.e., 0.5 Hz, and 1 Hz), it shows that the RBFNN-based controller contributes the majority of control efforts in the total nonlinear controller, and the RBFNN-based controller provides much more control efforts than the SMC (u_s). This also implies that the RBFNN in the proposed controller can help to reduce the required control effort and the chattering effect from the SMC while the system is tracking the high-frequency trajectories.

V. CONCLUSION

In this letter, an intelligent force controller is proposed for a USM-driven robotic system involving tool-soft tissue interaction. The controller is designed to get rid of the great challenges brought from such tool-soft tissue interaction due to the nonlinearity, viscoelasticity, and uncertainties of the soft environment. Firstly, the system model considering the HC contact model is built. Based on the system model, a learning-based force controller, consisting of a force feedforward plus feedback controller, an RBFNN-based controller, and an adaptive PI-type SMC, is proposed. The generality of the designed controller is analyzed through the Lyapunov method in detail. In the end, several experiments in the robotic prototype have been conducted. The experimental results illustrate that the proposed force controller can obtain good force tracking performance that is better than the conventional control method (e.g., PID controller) and another nonlinear control method (e.g., advanced SMC). The experimental results also show that the proposed controller can obtain guaranteed robustness to different soft environments. In addition, the good force track performance of the proposed controller with small force error can potentially benefit the surgical operation while the robotic system is working for tool-soft tissue interaction. Besides that, the potential future work can be integrating the ideas of optimal control (e.g., linear quadratic control) or more advanced SMC (e.g., terminal SMC) with the learning-based control to further improve the tracking control performance.

REFERENCES

[1] Y. He, B. Zhao, X. Qi, S. Li, Y. Yang, and Y. Hu, "Automatic surgical field of view control in robot-assisted nasal surgery," *IEEE Robot. Autom. Lett.*, vol. 6, no. 1, pp. 247–254, Jan. 2021.

[2] A. Ebrahimi *et al.*, "Real-time sclera force feedback for enabling safe robot-assisted vitreoretinal surgery," in *Proc. 40th Annu. Int. Conf. IEEE EMBC*, Honolulu, HI, USA, 2018, pp. 3650–3655.

[3] W. Liang, J. Ma, and K. K. Tan, "Contact force control on soft membrane for an ear surgical device," *IEEE Trans. Ind. Electron.*, vol. 65, no. 12, pp. 9593–9603, Dec. 2018.

[4] H. Choi, H.-S. Kwak, Y.-A. Lim, and H. Kim, "Surgical robot for single-incision laparoscopic surgery," *IEEE Trans. Biomed. Eng.*, vol. 61, no. 9, pp. 2458–2466, Sep. 2014.

[5] J. Guo, B. Xiao, and H. Ren, "Compensating uncertainties in force sensing for robotic-assisted palpation," *Appl. Sci.*, vol. 9, no. 12, 2019, Art. no. 2573, doi: 10.3390/app9122573.

[6] A. Attanasio *et al.*, "Autonomous tissue retraction in robotic assisted minimally invasive surgery: A feasibility study," *IEEE Robot. Autom. Lett.*, vol. 5, no. 4, pp. 2501–2508, Oct. 2020.

[7] H. Su *et al.*, "Asymmetric bimanual control of dual-arm serial manipulator for robot-assisted minimally invasive surgeries," *Sens. Mater.*, vol. 32, no. 4, pp. 1223–1233, 2020.

[8] S. G. Yuen, D. P. Perrin, N. V. Vasilyev, P. J. Del Nido, and R. D. Howe, "Force tracking with feed-forward motion estimation for beating heart surgery," *IEEE Trans. Robot.*, vol. 26, no. 5, pp. 888–896, Oct. 2010.

[9] A. Bajo and N. Simaan, "Hybrid motion/force control of multi-backbone continuum robots," *Int. J. Robot. Res.*, vol. 35, no. 4, pp. 422–434, 2016.

[10] Q. Huang, J. Lan, and X. Li, "Robotic arm based automatic ultrasound scanning for three-dimensional imaging," *IEEE Trans. Ind. Inform.*, vol. 15, no. 2, pp. 1173–1182, Feb. 2019.

[11] A. Ebrahimi, N. Patel, C. He, P. Gehlbach, M. Kobilarov, and I. Iordachita, "Adaptive control of sclera force and insertion depth for safe robot-assisted retinal surgery," in *Proc. Int. Conf. Robot. Autom.*, 2019, pp. 9073–9079.

[12] J. Guo, L. He, and S. Guo, "Study on force feedback control of the vascular interventional surgical robot based on fuzzy PID," in *Proc. IEEE Int. Conf. Mechatronics Autom.*, 2020, pp. 1710–1715.

[13] J. Florez, J. Szewczyk, and G. Morel, "An impedance control strategy for a hand-held instrument to compensate forphysiological motion," in *Proc. IEEE Int. Conf. Robot. Autom.*, 2012, pp. 1952–1957.

[14] M. Jolaei, A. Hooshiar, A. Sayadi, J. Dargahi, and M. Packirisamy, "Sensor-free force control of tendon-driven ablation catheters through position control and contact modeling," in *Proc. 42nd Annu. Int. Conf. IEEE EMBC*, 2020, pp. 5248–5251.

[15] M. Dominici, P. Poignet, and E. Dombre, "Compensation of physiological motion using linear predictive force control," in *Proc. IEEE Int. Conf. Intell. Robots Syst.*, 2010, pp. 1173–1178.

[16] M. Dominici, R. Cortesao, and C. Sousa, "Heart motion compensation for robotic-assisted surgery predictive approach vs active observer," in *Proc. IEEE Int. Conf. Robot. Autom.*, 2011, pp. 6252–6257.

[17] Z. Zarrouk, A. Chemori, and P. Poignet, "Adaptive force feedback control for 3D compensation of physiological motion in beating heart surgery," in *Proc. IEEE/RSJ Int. Conf. Intell. Robots Syst*, 2010, pp. 1856–1861.

[18] K. K. Tan, W. Liang, L. P. Pham, S. Huang, C. W. Gan, and H. Y. Lim, "Design of a surgical device for office-based myringotomy and grommet insertion for patients with otitis media with effusion," *J. Med. Devices*, vol. 8, no. 3, pp. 031001-1–12, 2014.

[19] K. K. Tan *et al.*, "Precision control of piezoelectric ultrasonic motor for myringotomy with tube insertion," *J. Dynamic Syst., Measurement, Control*, vol. 137, no. 6, pp. 064504-1–7, 2015.

[20] P. Moreira, N. Zemiti, C. Liu, and P. Poignet, "Viscoelastic model based force control for soft tissue interaction and its application in physiological motion compensation," *Comput. Methods Programs Biomed.*, vol. 116, no. 2, pp. 52–67, 2014.

[21] C. Yang, Y. Xie, S. Liu, and D. Sun, "Force modeling, identification, and feedback control of robot-assisted needle insertion: A survey of the literature," *Sensors*, vol. 18, no. 2, 2018, Art. no. 561, doi: 10.3390/s18020561.

[22] R. Schindeler and K. Hashtrudi-Zaad, "Online identification of environment hunt-crossley models using polynomial linearization," *IEEE Trans. Robot.*, vol. 34, no. 2, pp. 447–458, Apr. 2018.

[23] C. Ng, W. Liang, C. W. Gan, H. Y. Lim, and K. K. Tan, "Optimization of the penetrative path during grommet insertion in a robotic ear surgery," *Mechatronics*, vol. 60, pp. 1–14, 2019.

[24] O. Kuljaca, N. Swamy, F. L. Lewis, and C. M. Kwan, "Design and implementation of industrial neural network controller using backstepping," *IEEE Trans. Ind. Electron.*, vol. 50, no. 1, pp. 193–201, Feb. 2003.

[25] H. C. Liaw and B. Shirinzadeh, "Neural network motion tracking control of piezo-actuated flexure-based mechanisms for micro-/nanomanipulation," *IEEE/ASME Trans. Mechatronics*, vol. 14, no. 5, pp. 517–527, Oct. 2009.

[26] Y. Li and Q. Xu, "Adaptive sliding mode control with perturbation estimation and PID sliding surface for motion tracking of a piezo-driven micromanipulator," *IEEE Trans. Control Syst. Technol.*, vol. 18, no. 4, pp. 798–810, Jul. 2010.

[27] J. Lee, M. Jin, N. Kashiri, D. G. Caldwell, and N. G. Tsagarakis, "Inversion-free force tracking control of piezoelectric actuatorsusing fast finite-time integral terminal sliding-mode," *Mechatronics*, vol. 57, pp. 39–50, 2019.